FIRST DIRECT OBSERVATION OF A WAKEFIELD GENERATED WITH STRUCTURED LIGHT

A. Liberman*, A. Golovanov, A.-M. Talposi, S. Tata, and V. Malka
Weizmann Institute of Science, Rehovot, Israel
S. Smartsev
Laboratoire de Physique des 2 Infinis Irène Joliot-Curie, Orsay, France

Abstract

Since their inception, laser-wakefield accelerators (LWFAs) have shown their capability to produce high-quality, monoenergetic electron beams. Yet, the push toward higher electron energies and more efficient accelerators is constrained by several limitations. Foremost among these are the dephasing and diffraction limits. A promising strategy to address these issues involves using structured light to modulate the on-axis propagation velocity in LWFAs. By pairing the diffraction-resistant properties of Bessel beams with spatio-temporal pulse shaping, this approach offers an unprecedented combination of extended acceleration lengths and strong acceleration gradients.

Here we present the first experimental observation of wakefields driven by such structured, flying-focus beams. Spatio-temporally tailored pulses are directed through a specialized focusing mirror to form a quasi-Bessel beam, and the resulting wakefield is directly probed using femtosecond relativistic electron microscopy. Simulations corroborate the experimental data, offering novel insights into this underexplored regime. We show an experimental demonstration of the ability to modify the on-axis propagation velocity of the wakefield. We track the wakefield's evolution throughout the focal region and examine how specific spatio-temporal manipulations influence both its structure and propagation velocity. Finally, we present the first results using such wakefields to accelerate electrons. These findings establish a foundation for harnessing flying-focus-based strategies to overcome dephasing in LWFA.

INTRODUCTION

Since their inception [1], laser wakefield accelerators (LWFAs) have attracted considerable attention due to their capability to produce accelerating gradients far exceeding those of conventional radio-frequency accelerators [2, 3]. Over the past decades, LWFAs have successfully generated high-quality, quasi-monoenergetic electron beams [4–6], reaching energies as high as 10 GeV [7]. These systems have opened pathways toward a range of applications, including compact light sources [8, 9], advanced radiotherapy techniques [10], and experimental studies of strong-field quantum electrodynamics [11, 12]. Nevertheless, many envisioned applications require even higher electron energies. A key factor limiting further energy gain is dephasing—the mismatch between the velocity of the plasma wave and that of the electrons—which ultimately halts efficient acceleration [2, 13].

Various strategies have been proposed to alleviate dephasing. These include density-transition-based rephasing schemes [14, 15] and staged acceleration using multiple LWFA modules [16]. To date, the most effective approach has been to operate at reduced plasma density [7, 17], which decreases the velocity mismatch between the laser pulse and the electron bunch. While this method has enabled electron energies approaching 10 GeV [7], it comes at the cost of a reduced accelerating gradient [1]. Consequently, the laser must be guided over extended distances to counteract diffraction [13, 17]. Both the diminished gradient and the increased propagation length become more restrictive at higher target energies, as the acceleration length grows nonlinearly while the gradient continues to decrease [13].

An alternative approach to overcoming dephasing involves tailoring the structure of the driving laser field to control the effective on-axis velocity of the intensity peak, thereby synchronizing the wakefield with the electron bunch [18–22]. This concept is realized through the "flying focus," in which the focal region is extended over multiple Rayleigh lengths and different portions of the beam focus at distinct longitudinal positions with adjustable timing. Several implementations of this concept have been investigated, such as the interference of tilted laser pulses [20] and the combination of longitudinal chromatism with group-delay dispersion [18, 19]. However, these methods are challenging to implement at the high intensities required for LWFA operation.

A more experimentally viable realization of the flying focus for LWFAs employs spatio-temporal pulse shaping in conjunction with focusing optics designed to produce quasi-Bessel beams [21, 22]. In particular, the axiparabola [23, 24] introduces both focusing and controlled spherical aberrations. This engineered aberration extends the focal region [23] and modifies the temporal evolution of the on-axis intensity [21, 22]. Additional control can be achieved by imposing a radially dependent pulse-front delay through spatio-temporal shaping prior to focusing [21]. Numerical studies indicate that this could enable electron acceleration beyond 100 GeV in existing facilities [21, 22].

Here we report the experimental observation of wakefields driven by flying-focus pulses of this kind, conducted on the HIGGINS 2 × 100 TW laser system at the Weizmann Institute of Science. Spatio-temporally engineered laser pulses are focused with an axiparabola and the resulting

* aaronrafael.liberman@weizmann.ac.il

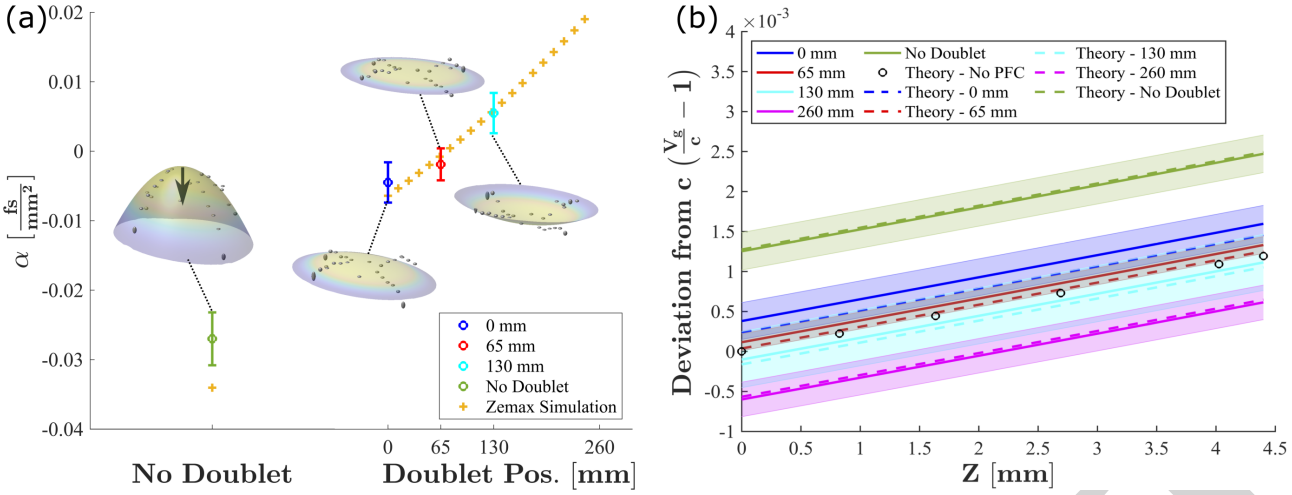

Figure 1: (a) Zemax simulations (orange) and experimentally retrieved pulse-front curvature (PFC) coefficients α for doublet positions of 0 mm (blue), 65 mm (red), and 130 mm (cyan), together with the no-doublet case (green). Insets display the reconstructed pulse-front delays: markers denote experimentally measured values at each spatial location, with their size indicating the associated uncertainty, while the colored surfaces represent fits to the radially dependent delay. The black arrow indicates the direction of pulse propagation. (b) On-axis propagation velocity of the intensity peak. Shaded regions indicate experimental uncertainties, dotted lines correspond to theoretical predictions, and black circles denote the zero-PFC (luminal) case. [Figure adapted from [25] licensed under CC BY 4.0.]

wakefield is directly resolved using femtosecond relativistic electron microscopy [26, 27]. The measurements are supported by simulations, which provide additional insight into this previously unexplored regime. We demonstrate experimental control over the on-axis propagation velocity of the laser driver [25] and of the wakefield and track its evolution throughout the extended focal region, revealing how tailored spatio-temporal structure governs both its morphology and dynamics. Furthermore, we present electron acceleration driven by these wakefields and evidence of the achievement of partial mitigation of dephasing [28, 29]. These results establish flying-focus-driven wakefields as a viable route toward overcoming dephasing in laser wakefield accelerators.

SPATIO-TEMPORAL PULSE CONTROL

The axiparabola employed in this experiment was characterized by a radial focusing profile of the form $f(r) = f_0 + \delta(r/R)^2$, where $\delta > 0$ denotes the focal depth, f_0 is the nominal focal length at the entrance of the extended focus, and R is the full beam radius. When pulse-front curvature is imposed on the incident beam, it introduces a radially varying temporal delay given by $\tau(r) = \alpha r^2$, where α, expressed in fs/mm^2, quantifies the magnitude of the PFC. For an axiparabola with this focusing profile and radial delay, the on-axis velocity of the intensity peak, expanded to second order, is given by [25]:

$$\frac{v_z}{c} = 1 - \frac{c\alpha R^2}{\delta} + \left(\frac{R^2}{2\delta f_0^2} - \frac{c\alpha R^4}{\delta^2 f_0^2}\right) z - \left(\left[\frac{R^2}{2\delta f_0^2} - \frac{c\alpha R^4}{\delta^2 f_0^2}\right]\frac{2}{f_0} - \frac{c\alpha R^6}{4\delta^3 f_0^4}\right) z^2 \quad (1)$$

where $z = f - f_0$. The optic used here had a nominal focal length of 480 mm, a focal depth of 5 mm, and an off-axis angle of 10°. It was designed to maintain an approximately uniform intensity throughout the focal region. Additional details of the optic are provided in Ref. [25].

Control over the pulse-front curvature (PFC) was achieved by introducing a custom-designed doublet lens within a beam-expansion telescope in the laser chain. This doublet was engineered to compensate for the intrinsic PFC arising from refractive beam expansion [30]. Its effect depends on the transverse size of the incident beam [31], enabling tunable PFC control by adjusting the doublet's position within the telescope. In this way, the native PFC of the beam can be partially or fully compensated, or even reversed in sign. Additional design details are provided in Refs. [25, 32]. The resulting PFC values were characterized using far-field beamlet cross-correlation (FFBCC) [32], a spatio-temporal diagnostic technique combining far-field interferometry with inverse Fourier transform spectroscopy.

Figure 1(a) presents the evolution of the pulse-front curvature (PFC) as a function of the doublet position within the beam expander, along with the case without the doublet. Measurements were performed for doublet positions of 0 mm, 65 mm, and 130 mm corresponding to the entrance, first quarter, and midpoint of the beam expander, respectively. In the absence of the doublet (green), a pronounced PFC is observed, originating from the refractive beam expansion in the laser system. Introducing the doublet at 0 mm (blue) leads to a substantial reduction in the PFC. At 65 mm (red), the PFC is nearly eliminated, while at 130 mm (cyan) its sign reverses, yielding a positive curvature. The orange crosses indicate values obtained from Ansys Zemax

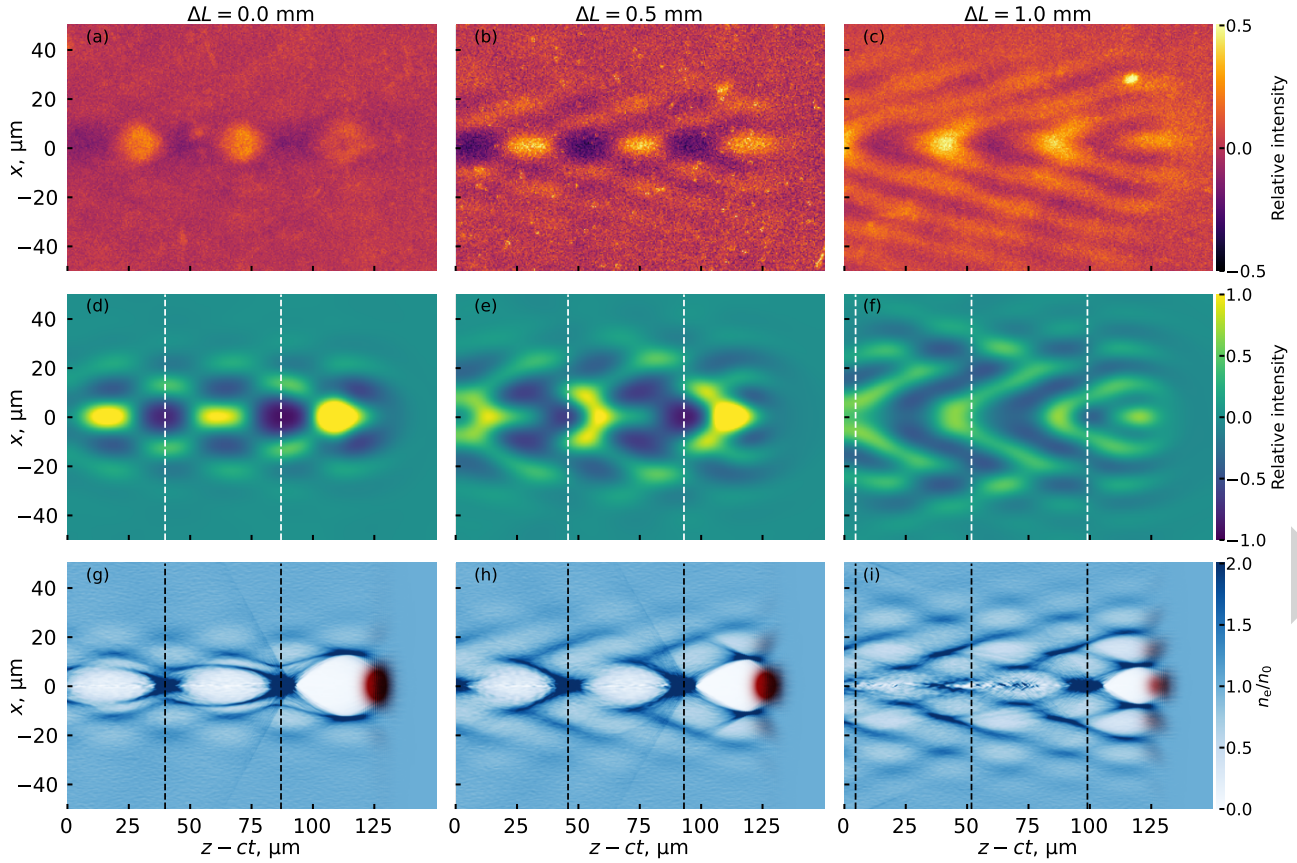

Figure 2: (a–c) Experimentally measured FREM images acquired at different relative positions ΔL along the focal region, illustrating the emergence and evolution of the characteristic V-shaped structure. (d–f) Corresponding simulated FREM images under comparable conditions and at similar locations within the nozzle. Panel (d) corresponds to a depth of 3.95 mm inside the nozzle (0.95 mm from the start of the focal region) in the PIC simulations. (g–i) Simulated relative electron density distributions, n_e/n_0, associated with the wakefields shown in (d–f). In panels (a–f), the color scale represents the normalized signal intensity on the detector, with zero corresponding to the unperturbed probe beam. The vertical lines in (d–i) indicate the plasma wavelength for a density of $n_0 = 5 \times 10^{17}$ cm^{-3}. In (g–i), the red shading denotes the intensity profile of the axiparabola-driven laser field. [Figure adapted from [26] licensed under CC BY 4.0.]

OpticStudio simulations. Insets in the figure show the reconstructed pulse fronts at each measurement point, with markers corresponding to data acquired via FFBCC.

The velocity measurement was done with a modified version of FFBCC. Data was taken for the arrival time of the annular slices of the beam at radial values: $r = 10.3, 14.5, 18.6,$ and 22.8 mm. These radial slices focused at the focal depth positions $z = 0.8, 1.6, 2.7,$ and 4.0 mm, respectively.

The deviation of the on-axis intensity propagation velocity from the speed of light is shown in Fig.1(b). In the absence of the doublet (green), the intrinsic PFC of the beam leads to superluminal propagation of the intensity peak. The solid curves correspond to the derivative of the fitted experimental data, while the dotted curves indicate the theoretical prediction from Eq.1; the shaded regions represent the experimental uncertainty. Introducing the doublet at 0 mm (blue) reduces the initial superluminal velocity, which continues to decrease as the doublet is translated to 65 mm (red), 130 mm (cyan), and 260 mm (magenta). The transition between 65 mm and 130 mm marks the inversion of the PFC sign. Consistent with expectations, the zero-PFC condition—indicated by black circles—lies between these positions. Beyond this point, the initial propagation velocity becomes subluminal.

DIRECT IMAGING WITH FREM

For this experiment the laser system delivered two temporally synchronized pulses with energies of 1 J on target and durations of 27 fs. Beam 1 was focused by the axiparabola onto a 15 mm-long supersonic slit nozzle (Jet 1), where it drove the flying-focus wakefield. In parallel, beam 2 was focused using a 1.5 m focal length off-axis parabolic mirror onto a supersonic converging–diverging nozzle (Jet 2), generating a separate wakefield that produced a femtosecond-duration electron bunch (the "probe" bunch).

The probe electrons were allowed to drift over 10 cm to increase their transverse size before intersecting the axiparabola-driven wakefield at near-normal incidence. As

the probe traversed the wake, the electromagnetic fields imparted transverse momentum modulations to the electrons. Following an additional 7 mm of free-space propagation, these momentum variations evolved into spatial density modulations within the beam. The modulated probe was subsequently recorded on a YAG scintillator, and the emitted radiation was imaged.

The flying-focus-driven wakefield was probed at multiple positions along the extended focal region by transversely steering the probe beam and compensating the corresponding temporal delay. Figures 2(a–c) present experimentally measured FREM images acquired at increasing depths within the gas nozzle. Panel (a) corresponds to the onset of the focal region, where the laser begins to drive a wakefield, while panels (b) and (c) are obtained at 0.5 mm and 1 mm further downstream, respectively. These snapshots reveal the progressive evolution of the wakefield structure along the propagation axis. In particular, a distinct V-shaped feature emerges near the axis: it is only weakly visible at the entrance to the focal region [Fig.2(a)], becomes more pronounced after 0.5 mm [Fig.2(b)], and dominates the signal after 1 mm of propagation [Fig. 2(c)].

To elucidate the underlying wakefield structure, particle-in-cell (PIC) simulations of the laser–plasma interaction were performed. The propagation of the laser pulse reflected from the axiparabola to the entrance of the gas jet was first modeled using the Axiprop code [24, 33], assuming an on-axis axiparabola with parameters matching the experiment. The resulting field distribution served as input to quasi-3D spectral PIC simulations carried out with FBPIC [34]. The interaction was modeled with a trapezoidal plasma density profile, including full ionization dynamics. The computed electromagnetic fields were subsequently used to generate synthetic FREM images by propagating a probe electron bunch with parameters comparable to those used experimentally through the simulated wake.

Figures 2(d–f) show the simulated FREM images at corresponding positions along the focal region. The simulations reproduce the key features and evolution observed experimentally, indicating that they capture the essential physics of this regime. This agreement enables a more detailed interpretation of the wakefield structure through the simulations. The corresponding electron density distributions, shown in Fig. 2(g–i), reveal that in addition to the central on-axis wake, off-axis wake structures develop as the pulse propagates along the focal line. Concurrently, the transverse extent of the on-axis wake decreases.

A key insight from comparing the simulated FREM images with the underlying wakefields is that the spatial periodicity observed in the FREM signal directly reflects the plasma wave structure. Since this periodicity is set by the plasma wavelength, it provides an in situ diagnostic of the plasma density [35, 36]. This correspondence is highlighted in Fig.2 by dashed lines, which demonstrate that the periodic modulations in the FREM images [Figs. 2(d–f)] are consistent with the longitudinal extent of the simulated wakefields [Figs. 2(g–i)].

ELECTRON ACCELERATION

For this experiment the laser system delivered one beam of 1.5 J on target. The beam was focused by the axiparabola onto a supersonic slit nozzle measuring 0.5 mm in width and 7 mm in length, with a 500 µm × 550 µm throat. This configuration produced a plasma with an electron density of approximately 4×10^{18} cm^{-3} at a height of 3 mm above the nozzle exit. Ionization injection was enabled using a gas mixture consisting of 97% helium and 3% nitrogen. The resulting electron beam was subsequently dispersed by a magnetic spectrometer and recorded on a Lanex screen for characterization.

The plasma density was inferred from interferometric measurements of the gas density profile and validated through fluid simulations performed with Ansys Fluent.

To model the electron acceleration process, Axiprop [24, 33] simulations were run in which a controlled pulse-front curvature (PFC) phase term was imposed prior to reflection. The resulting field distribution was then used as input for FPBIC [34] simulations. The plasma density profile was taken from Fluent simulations, with the gas initially treated as neutral to capture diffraction effects at larger radii where partial ionization may occur.

Electron acceleration was investigated for three distinct positions of the doublet within the beam expansion telescope, corresponding to its placement at the entrance (PFC value of $\alpha = -0.0045$), midpoint ($\alpha = 0.0055$), and exit ($\alpha = 0.0190$) of the system. As demonstrated in Ref. [26], changing the pulse-front curvature (PFC) tunes the wakefield velocity: negative PFC produces a faster wakefield, while positive PFC leads to slower wakefield.

Figure 3(a) presents the averaged electron energy spectrum above 225 MeV—highlighting the cutoff region—for 20 shots in the $\alpha = -0.0045$ case. The solid curve represents the mean charge distribution, while the shaded region indicates the RMS shot-to-shot variation. Equivalent spectra for $\alpha = 0.0055$ and $\alpha = 0.0190$ are shown in Figs.3(b) and (c), respectively. A direct comparison of the averaged spectra is given in Fig.3(d), revealing a clear dependence of the cutoff energy on the wakefield velocity. Over the acceleration, the cutoff shifts by approximately 50 MeV, increasing from ~350 MeV for the slowest wakefield ($\alpha = 0.0190$, orange) to ~400 MeV for the fastest ($\alpha = -0.0045$, green).

Figure 3(e) shows the corresponding spectra obtained from PIC simulations for the same configurations. The simulated results reproduce the dependence on the wakefield velocity seen in the experimentally measured spectra. In the simulations, a shift of approximately 45 MeV is observed between the $\alpha = -0.0045$ and $\alpha = 0.0190$ cases. The higher cutoff energies observed in the simulations—reaching approximately 485 MeV for α = -0.0045 and 440 MeV for $\alpha = 0.0190$—can be attributed to the idealized conditions employed, including a simplified gas density profile and an aberration-free axiparabola. The increased charge predicted by the simulations likely arises from these same factors. Despite these quantitative differences, the simulations

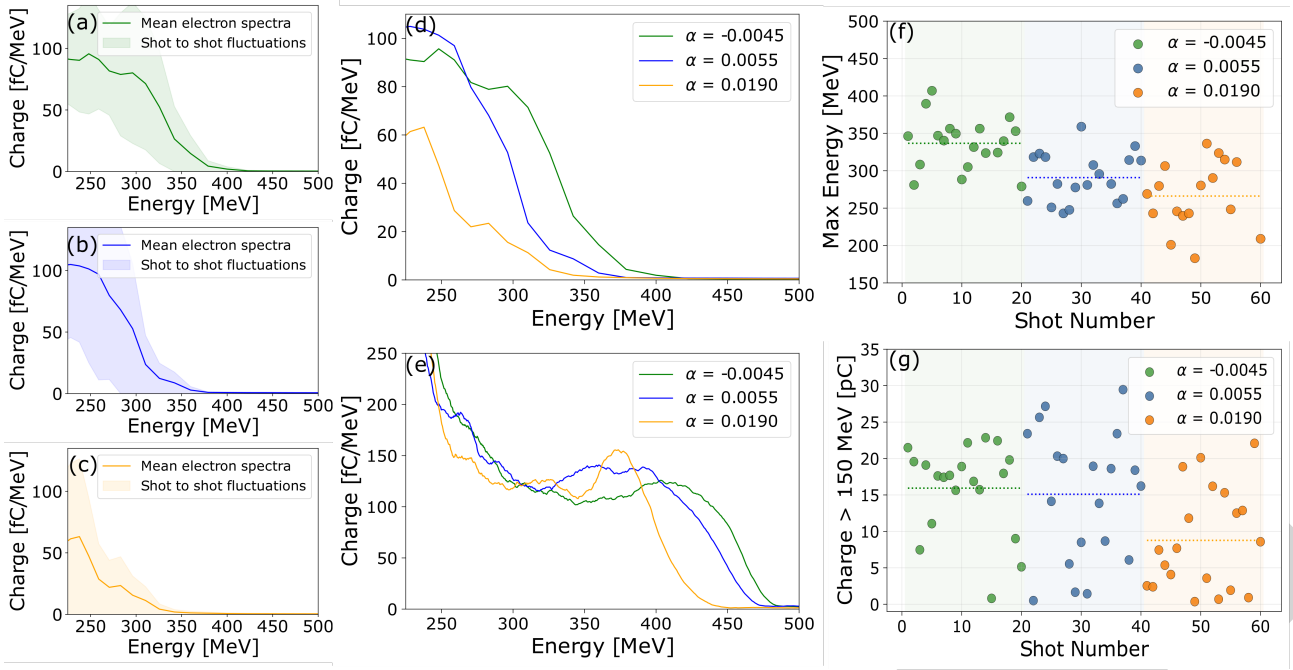

Figure 3: (a–c) Electron energy spectra above 225 MeV, averaged over 20 shots, for $\alpha = -0.0045$ (b, green), $\alpha = 0.0055$ (c, blue), and $\alpha = 0.0190$ (d, orange). The horizontal axis shows electron energy, while the vertical axis represents charge density. Shaded regions indicate the RMS shot-to-shot fluctuations.(d) Direct comparison of the averaged spectra for the three PFC configurations.(e) Corresponding electron spectra obtained from PIC simulations for the same cases.(f) Shot-to-shot variation of the maximum electron energy for each configuration; dotted lines denote the mean maximum energy.(g) Shot-to-shot variation of the total charge above 150 MeV; dotted lines indicate the mean charge for each case. [Figure adapted from [29] licensed under CC BY 4.0.]

and experimental results are in strong qualitative agreement, capturing the same underlying physics and clearly demonstrating the influence of wakefield velocity on the electron acceleration process.

The shot-to-shot distribution of maximum electron energies is shown in Fig. 3(f), with dashed lines indicating the mean value for each configuration. The separation between the distributions is statistically significant, with a p-value of 4×10^{-4}, corresponding to a significance exceeding 3.5σ between the $\alpha = -0.0045$ and $\alpha = 0.0055$ cases, and even higher significance when compared to the $\alpha = 0.0190$ case.

Figure 3(g) presents the shot-to-shot variation of the charge above 150 MeV, with dashed lines marking the mean values. Although substantial charge fluctuations are observed across all configurations, the shift in cutoff energy remains robust. This decoupling of energy gain from charge variation suggests that the observed effect is not driven by beam loading or changes in the injection process, but rather by the controlled variation of the propagation velocity.

CONCLUSION

The proof-of-concept experiments outlined in this work–the successful manipulation of the on-axis propagation velocity of intensity, the direct probing of the flying-focus generated wakefield, and the demonstration of electron acceleration with such a wakefield–represent important steps towards the realization of dephasingless LWFA. Yet, challenges remain that must be tackled before a robust mitigation of dephasing can be achieved. These include optimizing the propagation velocity of the wakefield–something complicated by the non-trivial translation of the vacuum velocity of the pulse into in-plasma velocity of the wakefield–and increasing the stability of the wakefield over the course of the acceleration. Optimizing these required further understanding of the wakefield behavior and finer control and metrology of the spatio-temporal pulse profile.

Technologies for spatio-temporal metrology and control are advancing rapidly, driven by the emergence of single-shot diagnostic techniques [37, 38] and the development of meta-optical elements capable of precise light-field structuring at high intensities [39]. These capabilities open a pathway toward the realization of stable, tunable flying-focus wakefields optimized to mitigate dephasing, with the potential to significantly extend the achievable energy range of LWFAs [21, 22]. Beyond electron acceleration, such approaches may be generalized to other regimes, including laser-driven ion acceleration [40] and more complex wakefield geometries, such as helical-beam-driven LWFAs for positron acceleration [41]

REFERENCES

[1] T. Tajima and JM. Dawson, “Laser electron accelerator”, *Physical Review Letters*, vol. 43, no. 4, 1979.

[2] C. Joshi, W. B. Mori, T. Katsouleas, J. M. Dawson, J. M. Kindel, and D. W. Forslund, "Ultrahigh gradient particle acceleration by intense laser-driven plasma density waves", *Nature*, vol. 311, pp. 525–529, Oct. 1984. doi:10.1038/311525a0

[3] A. Modena *et al.*, "Electron acceleration from the breaking of relativistic plasma waves", *Nature*, vol. 377, pp. 606–608, Oct. 1995. doi:10.1038/377606a0

[4] J. Faure *et al.*, "A laser–plasma accelerator producing monoenergetic electron beams", *Nature*, vol. 431, pp. 541–544, Sep. 2004. doi:10.1038/nature02963

[5] C. G. R. Geddes *et al.*, "High-quality electron beams from a laser wakefield accelerator using plasma-channel guiding", *Nature*, vol. 431, pp. 538–541, Sep. 2004. doi:10.1038/nature02900

[6] S. P. D. Mangles *et al.*, "Monoenergetic beams of relativistic electrons from intense laser–plasma interactions", *Nature*, vol. 431, pp. 535–538, Sep. 2004. doi:10.1038/nature02939

[7] A. Picksley *et al.*, "Matched guiding and controlled injection in dark-current-free, 10-gev-class, channel-guided laser-plasma accelerators", *Phys. Rev. Lett.*, vol. 133, no. 25, p. 255001, Dec. 2024. doi:10.1103/PhysRevLett.133.255001

[8] W. Wang *et al.*, "Free-electron lasing at 27 nanometres based on a laser wakefield accelerator", *Nature*, vol. 595, pp. 516–520, Jul. 2021. doi:10.1038/s41586-021-03678-x

[9] M. Labat *et al.*, "Seeded free-electron laser driven by a compact laser plasma accelerator", *Nature Photonics*, vol. 17, pp. 150–156, Dec. 2022. doi:10.1038/s41566-022-01104-w

[10] Y. Glinec, J. Faure, V. Malka, T. Fuchs, H. Szymanowski, and U. Oelfke, "Radiotherapy with laser-plasma accelerators: monte Carlo simulation of dose deposited by an experimental quasimonoenergetic electron beam", *Medical Physics*, vol. 33, pp. 155–162, Jan. 2006. doi:10.1118/1.2140115

[11] M. Mirzaie *et al.*, "All-optical nonlinear compton scattering performed with a multi-petawatt laser", *Nature Photonics*, vol. 18, pp. 1212–1217, Oct. 2024. doi:10.1038/s41566-024-01550-8

[12] L. Collaboration, "Technical design report for the luxe experiment", *European Physics Journal Special Topics*, vol. 233, pp. 1709–1974, Oct. 2024. doi:10.1140/epjs/s11734-024-01164-9

[13] E. Esarey, C. B. Schroeder, and W. P. Leemans, "Physics of laser-driven plasma-based electron accelerators", *Rev. Mod. Phys.*, vol. 81, no. 3, pp. 1229–1285, Aug. 2009. doi:10.1103/RevModPhys.81.1229

[14] P. Sprangle *et al.*, "Wakefield generation and GeV acceleration in tapered plasma channels", *Physical Review E*, vol. 63, no. 5, p. 056405, Apr. 2001. doi:10.1103/PhysRevE.63.056405

[15] E. Guillaume *et al.*, "Electron rephasing in a laser-wakefield accelerator", *Physical Review Letters*, vol. 115, no. 15, p. 155002, Oct. 2015. doi:10.1103/PhysRevLett.115.155002

[16] W. Leemans and E. Esarey, "Laser-driven plasma-wave electron accelerators", *Physics Today*, vol. 62, no. 3, pp. 44–49, Mar. 2009. doi:10.1063/1.3099645

[17] W. P. Leemans *et al.*, "Gev electron beams from a centimetre-scale accelerator", *Nature Physics*, vol. 2, pp. 696–699, Sep. 2006. doi:10.1038/nphys418

[18] A. Sainte-Marie, O. Gobert, and F. Quere, "Controlling the velocity of ultrashort light pulses in vacuum through spatio-temporal couplings", *Optica*, vol. 4, no. 10, pp. 1298–1304, Oct. 2017. doi:10.1364/OPTICA.4.001298

[19] D. H. Froula *et al.*, "Spatiotemporal control of laser intensity", *Nature Photonics*, vol. 12, pp. 262–265, May 2018. doi:10.1038/s41566-018-0121-8

[20] A. Debus *et al.*, "Circumventing the dephasing and depletion limits of laser-wakefield acceleration", *Physical Review X*, vol. 9, no. 3, p. 031044, Sep. 2019. doi:10.1103/PhysRevX.9.031044

[21] C. Caizergues, S. Smartsev, V. Malka, and C. Thaury, "Phase-locked laser-wakefield electron acceleration", *Nature Photonics*, vol. 14, pp. 475–479, Aug. 2020. doi:10.1038/s41566-020-0657-2

[22] J. P. Palastro, J. L. Shaw, D. Ramsey, T. T. Simpson, and D. H. Froula, "Dephasingless laser wakefield acceleration", *Physical Review Letters*, vol. 124, p. 134802, Mar. 2020. doi:10.1103/PhysRevLett.124.134802

[23] S. Smartsev *et al.*, "Axiparabola: a long-focal-depth, high-resolution mirror for broadband high-intensity lasers", *Optics Letters*, vol. 44, no. 14, pp. 3414–3417, Jul. 2020. doi:10.1364/OL.44.003414

[24] K. Oubrerie, I. A. Andriyash, R. Lahaye, S. Smartsev, V. Malka, and C. Thaury, "Axiparabola: a new tool for high-intensity optics", *Journal of Optics*, vol. 24, no. 4, Mar. 2022. doi:10.1088/2040-8986/ac57d2

[25] A. Liberman *et al.*, "Use of spatiotemporal couplings and an axiparabola to control the velocity of peak intensity", *Opt. Lett.*, vol. 49, no. 4, pp. 814–817, Feb. 2024. doi:10.1364/OL.507713

[26] A. Liberman *et al.*, "Direct observation of a wakefield generated with structured light", *Nature Communications*, vol. 16, no. 10957, Dec. 2025. doi:10.1038/s41467-025-66056-5

[27] A. Liberman, A. Golovanov, S. Tata, A.-M. Talposi, and V. Malka, "Probing flying-focus wakefields", *Reports on Progress in Physics*, vol. 89, no. 3, p. 038501, Mar. 2026. doi:10.1088/1361-6633/ae4ff0

[28] A. Liberman *et al.*, "First electrons from axiparabola-based lwfa", in *CLEO 2024*, ATh3H.1, 2024. https://opg.optica.org/abstract.cfm?URI=CLEO_AT-2024-ATh3H.1

[29] A. Liberman, A. Golovanov, S. Smartsev, A.-M. Talposi, S. Tata, and V. Malka, "First electron acceleration in a tunable-velocity laser wakefield", *Phys. Rev. Res.*, vol. 8, no. 2, p. L022001, Apr. 2026. doi:10.1103/x5pr-mdvj

[30] R. Netz and T. Feurer, "Diffraction of ultrashort laser pulses and applications for measuring pulse front distortion and pulse width", *Applied Physics B*, vol. 70, pp. 813–819, 2000.

[31] A. Kabacinski *et al.*, "Measurement and control of main spatio-temporal couplings in a CPA laser chain", *Journal of Optics*, vol. 23, no. 6, 06LT01, Apr. 2021. doi:10.1088/2040-8986/abf88f

[32] S. Smartsev *et al.*, "Characterization of spatiotemporal couplings with far-field beamlet cross-correlation", *Journal of Optics*, vol. 24, no. 11, p. 115503, Oct. 2022. doi:10.1088/2040-8986/ac9631

[33] I. Andriyash, Axiprop, 2024. https://github.com/hightower8083/axiprop

[34] R. Lehe, M. Kirchen, I. A. Andriyash, B. B. Godfrey, and J.-L. Vay, "A spectral, quasi-cylindrical and dispersion-free particle-in-cell algorithm", *Computer Physics Communications*, vol. 203, pp. 66–82, 2016. doi:https://doi.org/10.1016/j.cpc.2016.02.007

[35] F. F. Chen, *Introduction to plasma physics and controlled fusion*. New York: Plenum, 1983.

[36] Y. Wan *et al.*, "Femtosecond electron microscopy of relativistic electron bunches", *Light: Science & Applications*, vol. 12, no. 1, p. 116, 2023. doi:10.1038/s41377-023-01142-1

[37] S. Smartsev *et al.*, "Simple few-shot method for spectrally resolving the wavefront of an ultrashort laser pulse", *Opt. Lett.*, vol. 49, no. 8, pp. 1900–1903, Apr. 2024. doi:10.1364/OL.502000

[38] S. Howard *et al.*, "Single-shot spatiotemporal vector field measurements of petawatt laser pulses", *Nature Photonics*, vol. 19, pp. 898–905, Jun. 2025. doi:10.1038/s41566-025-01698-x

[39] B. Oliveira *et al.*, "High-aspect-ratio, ultratall silica metaoptics for high-intensity structured light", *Optica*, vol. 12, no. 5, pp. 713–719, May 2025. doi:10.1364/OPTICA.559278

[40] Z. Gong, S. Cao, J. P. Palastro, and M. R. Edwards, "Laser wakefield acceleration of ions with a transverse flying focus", *Phys. Rev. Lett.*, vol. 133, no. 26, p. 265002, Dec. 2024. doi:10.1103/PhysRevLett.133.265002

[41] J. Vieira and J. T. Mendonça, "Nonlinear laser driven donut wakefields for positron and electron acceleration", *Physical Review Letters*, vol. 112, no. 21, p. 215001, May 2014. doi:10.1103/PhysRevLett.112.215001